

Isospin ferromagnetism and momentum polarization in bilayer graphene

Zhiyu Dong, Margarita Davydova, Makinde Ogunnaike, Leonid Levitov
Massachusetts Institute of Technology, Cambridge, Massachusetts 02139, USA
 (Dated: March 22, 2022)

Electron bands in Bernal-stacked (nontwisted) graphene bilayers in a transverse electric field feature field-tunable bandgaps and uniquely weak carrier dispersion. The effects of electron interactions are sharply enhanced as the field increases, leading to a cascade of correlated phases exhibiting isospin (spin-valley) and momentum polarization orders. Momentum polarization, driven by exchange interactions, originates from a “flocking” effect, wherein all carriers condense into one, two or three pockets produced by the trigonal warping of the electron bands. The isospin-polarized phases mimic many aspects of the phases found in moiré graphene. The momentum-polarized phases, to the contrary, have symmetry lower than that of the isospin-polarized phases in moiré bands. We identify effects that can serve as probes of these orders, such as electronic nematicity, incommensurate Kekulé-type density waves and a $B = 0$ anomalous Hall response.

Narrow bands in moiré graphene[1, 2] host a variety of strongly correlated phases with exotic properties that can be accessed by tuning external fields and carrier density[3–24]. These findings prompted questions about the existence of other narrow band types with similar properties, and about other symmetry breaking types and new orders achievable in this manner. Recently, two nontwisted graphene multilayers—Bernal-stacked bilayers and abc trilayers—have been identified as systems showing cascades of ordered phases resembling those seen in moiré graphene[25, 26]. These system feature electron bands with field-tunable bandgaps and dispersion that flattens out quickly as the field increases. Carriers in these bands become nearly dispersionless at large fields, forming strongly interacting systems with interesting properties[27, 28]. Recent measurements[25, 26] demonstrated cascades of isospin-ordered phases resembling those seen in moiré graphene[29–33].

In this paper, starting from a simple framework for the interaction effects, we predict new order types with properties considerably more rich than those of isospin-ordered phases. We focus on the Bernal-stacked bilayer graphene in a transverse electric field, arguably the simplest known system in which bands can be flattened by applying external fields. This system hosts Bloch bands with field-tunable bandgap and dispersion that flattens out quickly as the field increases. Expectedly, strong interactions of carriers in flattened bands drive isospin (spin-valley) polarization instability and a cascade of phase transitions between states with different polarization types, resembling those known previously[29–33]. Thus behavior is illustrated in Fig.1 a).

Strikingly, a sharp change in behavior occurs at lower densities and stronger fields, where interactions lead to an isospin-polarized Fermi sea break-up and spontaneous momentum polarization, as illustrated in Fig.1 b). Momentum polarization originates from exchange-induced “flocking” effect, wherein all carriers condense into one, two or three pockets shifted towards band minima produced by the trigonal warping interactions. The momentum-polarized phases have symmetry lower than that of the isospin-polarized phases. We describe unique

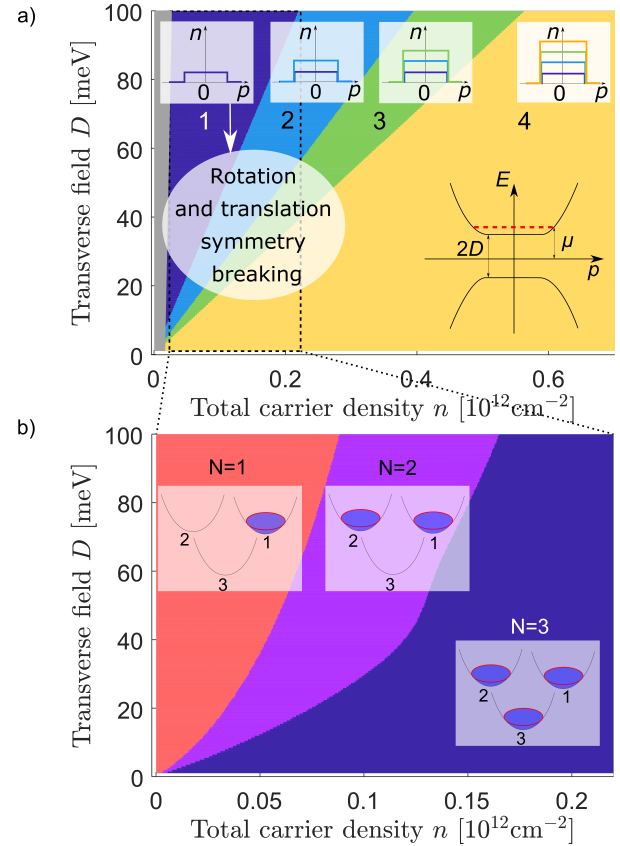


FIG. 1. a) Phase diagram for different isospin (valley and spin) orders in a lightly-doped field-biased BG band. Carriers form Fermi seas with the degree of isospin polarization increasing upon field bias growing. States with different numbers of isospin species, pictured in the insets, are found in the four regions of the phase diagram obtained using realistic parameters. Polarization degree varies from one layer (fully polarized) to four layers (unpolarized) [see text beneath Eq.(7)]. b) Level-two symmetry breaking occurring in a dashed box marked in a). Different orders arise due to the Fermi sea spontaneously breaking into $N = 1, 2$ or 3 pockets and shifting to different band minima [see text after Eq.(17)]. Pocket-polarized states feature electronic nematicity, incommensurate density waves and anomalous Hall response.

signatures of these orders, such as electronic nematicity and incommensurate Kekulé-type density waves. Furthermore, as discussed below, trigonal warping effects lead to Berry curvature redistributing throughout the band such that momentum-polarized states feature an enhanced anomalous Hall response (see Fig.2). An abrupt onset of a $B = 0$ Hall effect, along with anisotropy of transport due to electronic nematicity, will provide clear signatures of momentum-polarized ordered states.

The field-biased BG band is readily described by a parabolic Dirac band with field-tunable gap, accounting for low-energy states near K and K' points:

$$H_0 = \sum_{\mathbf{p}} \Psi_{\mathbf{p}}^\dagger h_0(\mathbf{p}) \Psi_{\mathbf{p}}, \quad (1)$$

$$h_0(\mathbf{p}) = -\frac{p_1^2 - p_2^2}{2m} 1_\tau \sigma_1 - \frac{2p_1 p_2}{2m} \tau_3 \sigma_2 + D 1_\tau \sigma_3$$

where $\Psi_{\mathbf{p}} = (\psi_{AK\mathbf{p}}, \psi_{BK\mathbf{p}}, \psi_{AK'\mathbf{p}}, \psi_{BK'\mathbf{p}})^T$, $\tau_{1,2,3}$ and $\sigma_{1,2,3}$ are the Pauli matrices acting on the valley and sublattice(layer) degrees of freedom, respectively. For conciseness, we have suppressed the spin indices for now, as the spin-orbit coupling is negligible. Here, the value of m is given by the experiment $m = 0.028m_e$ [36, 37]. The quantity D is the interlayer bias generated by the transverse electric field. Other subleading terms[40], including trigonal warping, are ignored for now as we focus on understanding the emergence of the ordered phases in $SU(4)$ -symmetric model. Subsequently, we will refine our picture by including the other relevant terms in the single-particle Hamiltonian.

Here, we will be interested in the regime where the field-induced bandgap $2D$ is large compared to the carrier kinetic energy (see inset in Fig. 1 a)). In this regime the upper and lower bands, flattened and separated by the energy $2D \gg \mu$, effectively decouple. We therefore project the problem onto the conduction band [41]

$$E(\mathbf{p}) = \sqrt{D^2 + \left(\frac{p^2}{2m}\right)^2} \quad (2)$$

We take the electron-electron interaction to be a density-density coupling of carriers in the conduction band,

$$\tilde{H}_{int} = \sum_{\mathbf{p}\mathbf{p}'\mathbf{q}} V_{\mathbf{q}} \tilde{\psi}_{i,\mathbf{p}}^\dagger \tilde{\psi}_{j,\mathbf{p}'}^\dagger \tilde{\psi}_{j,\mathbf{p}'+\mathbf{q}} \tilde{\psi}_{i,\mathbf{p}+\mathbf{q}}, \quad (3)$$

where $\tilde{\psi}_{i,\mathbf{p}}$ are field operators of conduction electrons, where i and j label the isospin components $K \uparrow$, $K \downarrow$, $K' \uparrow$, $K' \downarrow$. This Hamiltonian has an isospin $SU(4)$ symmetry.

To gain insight into the parameter regime for isospin polarization occurs we use a simple constant interaction model, refining it in the subsequent analysis of momentum polarized order. The isospin order is a result of Stoner instability arising from the exchange energy,

which can be written as

$$E_{ex} = -\frac{1}{2} \sum_{i\mathbf{p}\mathbf{p}'} V_{\mathbf{p}-\mathbf{p}'} n_{i\mathbf{p}} n_{i\mathbf{p}'}, \quad (4)$$

where i is the isospin index, same as in Eq.(3). Below, for simplicity, we model the interaction as a local interaction, $V_{\mathbf{p}-\mathbf{p}'} = V$. The onset of $SU(4)$ isospin polarization is approximately determined through the Stoner criterion:

$$V\nu = 1, \quad (5)$$

where the density of states ν in our model is given by

$$\nu = \frac{m}{2\pi} \frac{\mu}{\sqrt{\mu^2 - D^2}} = \frac{m^2}{(2\pi)^2} \frac{D}{n}, \quad (6)$$

where we have used the expression for the electron density in the single-electron picture $n = \frac{m}{2\pi} \sqrt{\mu^2 - D^2}$ and assumed that the chemical potential lies near the bottom of the band $\mu \sim D$. Using these, we can estimate the carrier density at the onset of the Stoner instability:

$$n_D = \frac{Vm^2D}{(2\pi)^2} \quad (7)$$

Thus, we find that the carrier density at the phase transition is linear in D . Using realistic parameters for Bernal-stacked graphene: $m = 0.028m_e$, $V = 1000 \text{ meV nm}^2$ [see [41] for a detailed discussion], this simple model predicts an isospin ordering transition at the carrier density $n_D \sim 10^{12} \text{ cm}^{-2}$ around a large but experimentally achievable values of the interlayer bias $D = 100 \text{ meV}$.

The resulting phase diagram is shown in Fig. 1 a). We obtain this phase diagram by numerically comparing the energies of the candidate configurations where either one, two, three or all four isospin species are at least partially populated. The inset at the lower right corner shows a schematic of electron dispersion near charge neutrality, in which the red dashed line represents the Fermi level. The yellow area represents the disordered phase where all four isospin species are equally filled. Purple, light blue and green represent ordered states. The numbers 1...4 in the figure label the numbers of species in each phase. We will refer to the three isospin ordered phases (from left to right in Fig. 1) as phase 1, phase 2, and phase 3, respectively. The inset at the top illustrates the wedding-cake structure of electron distribution in each of the phases. Outlines of different colors represent the Fermi seas of each isospin component. The gray part is a schematic of the band insulator phase near charge neutrality, which is not of our interest. In the low density regime represented by dashed rectangle, as we will see shortly, the subleading terms in the Hamiltonian results in an interesting Fermi sea topology, which gives rise to a new instability and breaks symmetry further. We will look into the details of it later when we discuss Fig. 1 b).

Because of $SU(4)$ symmetry, the phase diagram Fig. 1 a) is blind to the isospin orientations of the order parameters due to $SU(4)$ invariance of our model. However, in

reality, other terms in the Hamiltonian, such as intervalley scattering, can lift the $SU(4)$ degeneracy and favor certain orientation in isospin space. The analysis of such $SU(4)$ anisotropy is beyond the scope of this paper.

Crucially, we can understand the symmetry aspects of different orders regardless of detailed knowledge of which order ultimately wins. Below, we describe the possible order types, classify them through the symmetry of our problem. For simplicity, we focus on the case of phase 1, where only one of the isospin species is populated. Other orders can be studied in a similar manner. In this phase the order parameter is simply a projection onto the state with a given valley-spin orientation. Therefore, it takes the form of

$$O_1 = |v\rangle\langle v| \quad (8)$$

where v is an arbitrary normalized complex-valued four-component spinor in the isospin space, $|v\rangle = (\alpha_1|u_1\rangle, \alpha_2|u_2\rangle)^T$ where $|u_1\rangle, |u_2\rangle$ are arbitrary normalized two-component state vectors in the spin subspace, α_1, α_2 are positive real numbers, $\alpha_1^2 + \alpha_2^2 = 1$. Overall phases are absorbed in $|u_1\rangle$ and $|u_2\rangle$. The symmetry analysis of the Pauli matrices in valley basis (see Table I) indicates that $\tau_{1,2}$ and τ_3 transform under different irreducible representations. Thus, an order parameter containing $\tau_{1,2}$ matrices and another one containing τ_3 corresponds to different broken symmetries. Therefore, to classify orders by symmetry, we look for the order parameter O that contains τ_3 or $\tau_{1,2}$ matrices only, but not a mixture of τ_3 and $\tau_{1,2}$. This gives two possible types of the order parameter with distinct symmetry: $O_1^z = \frac{1}{4}(1 \pm \tau_3)(1 + \mathbf{s} \cdot \mathbf{m})$ and $O_1^{xy} = \frac{1}{4}(1 + \gamma_1\tau_1 + \gamma_2\tau_2)(1 + \mathbf{s} \cdot \mathbf{m})$. Here, \mathbf{m} is an arbitrary vector determining the spin direction, and (γ_1, γ_2) is an arbitrary normalized real-valued vector. The order O_1^z represents a valley imbalance order, which transforms under $A_{2,\Gamma}$ and thus, features a breakdown of the mirror symmetry that swaps the two valleys. The other option, O_1^{xy} , corresponds to the intervalley coherent order that transforms under $E_{\pm K}$. It breaks the three-fold rotation, reflection and translation symmetries of the original model. This aspect clearly differentiates the AB bilayer graphene from the case of ABC trilayer: in the latter, the intervalley coherent state does not break the C_3 rotation symmetry[27]. The symmetry classification of possible orders in AB bilayer graphene is summarized in Table I.

Our symmetry analysis allows us to identify two observables that distinguish the valley imbalance and intervalley coherent orders in phase 1. These are anisotropy of conductivity and a spatial charge density wave modulation. For valley imbalance order O_1^z , neither rotation nor translation symmetry of the space group is broken, so the conductivity is isotropic and there is no spatial pattern. In comparison, for the valley coherence order O_1^{xy} , both rotation and translation symmetries are broken. The broken rotation symmetry leads to an anisotropic conductivity, whereas the broken translation symmetry leads to a spatial pattern with momentum $2K$, i.e. a Kekulé charge

density wave. On a different note, the temporal symmetry can be probed by the Hall conductance. For the valley imbalance order O_1^z where time reversal symmetry is broken, the Hall conductivity is nonvanishing. In comparison, the intervalley coherent order O_1^{xy} preserves time reversal symmetry which guarantees a vanishing Hall conductance. These observables are summarized in the last three columns in Table I.

Next, we proceed to explore the momentum-polarized ordered states that are unique to the biased BG. These orders arise through an instability in which the isospin-polarized Fermi sea breaks up into several distinct pockets that shift towards minima of the conduction band.

We start with a qualitative discussion of how this instability comes into play. There is a strong anisotropy in realistic BLG band structure at small momenta due to the trigonal warping term, which is not included in the minimal description of band structure Eq. (1). This anisotropy leads to a three-pocket shape of Fermi surface in the regime of extremely low carrier density. As a result, for each isospin, instead of uniformly filling all three pockets, there are three candidate electron configurations for the ground state, in which either one, two or all three pockets are filled. Which one wins is determined by the competition between the kinetic and the exchange energy. The kinetic energy favors the configuration where all pockets are uniformly filled, whereas the exchange energy is optimized when electrons are placed in the same pocket, so long as the interpocket interaction is weaker than the intrapocket one. We give an estimate of the scale at which this competition occurs. The total single-particle kinetic energy penalty for a one-pocket state can be estimated as

$$E_K \sim \frac{n^2}{2\nu_*} \quad (9)$$

where $\nu_* \sim 5 \times 10^{-5} \text{ meV}^{-1} \text{ nm}^{-2}$ is an estimate of the density of states at the bottom of a single pocket. To study the pocket polarization, we take into account the momentum dependence of the interaction. Then the exchange part of the energy is:

$$E_{ex} \sim -\frac{2\pi e^2}{\kappa|p|}n^2 \sim -\frac{\sqrt{\pi}}{\kappa}e^2n^{\frac{3}{2}} \quad (10)$$

where we introduced dielectric constant κ to effectively represent the screening in experiments. We estimate the characteristic momentum scale $|p|$ as $|p| \sim \sqrt{4\pi n}$. As a result, the exchange energy dominates at sufficiently small density $n \lesssim n_* = \frac{4\pi}{\kappa^2}e^4\nu^2 \sim 0.1 \times 10^{12} \text{ cm}^{-2}$, where we have used the realistic values of D, ν : $D \sim 100 \text{ meV}$, $\nu = 5 \times 10^{-5} \text{ meV}^{-1} \text{ nm}^{-2}$, and assumed $\kappa \sim 5$ which is similar to dielectric constant in monolayer graphene. The realistic values of κ depends on the experimental setup.

Next, we consider a simple model that accounts for pocket ordering, and work out a phase diagram for realistic system parameters. Consider a simple low-energy model consisting of three parabolic bands representing the three electron pockets in field-biased BG:

irreps	matrices	O_1	broken symmetries	Ohmic conductivity	spatial modulation	Hall conductivity
$A_{2,\Gamma}$, 1D	τ_3	$P_\tau^{\pm z} P_s^{\mathbf{m}}$	mirror, time reversal	isotropic	none	nonvanishing
$E_{\pm K}$, 2D	(τ_1, τ_2)	$P_\tau^\gamma P_s^{\mathbf{m}}$	rotation, mirror, translation	anisotropic	Kekulé order	vanishing

TABLE I. Symmetry classification of different momentum-independent isospin orders. We find two real irreducible representations (irreps) under which the Pauli matrices in valley basis (the second column) transform. Other irreps of the space group are not realized by momentum-independent orders. In the first column, d labels the dimension. In the third column, we have defined projection operators in valley and spin space as follows: $P_\tau^{\pm z} = \frac{1}{2}(1 \pm \tau_3)$, $P_\tau^\gamma = \frac{1}{2}(1 + \gamma_1 \tau_1 + \gamma_2 \tau_2)$, $P_s^{\mathbf{m}} = \frac{1}{2}(1 + \mathbf{s} \cdot \mathbf{m})$, where $\gamma = (\gamma_1, \gamma_2)^T$ is an arbitrary real vector in xy plane, $\mathbf{m} = (m_1, m_2, m_3)^T$ is an arbitrary three-dimensional real vector [see the discussion in the main text].

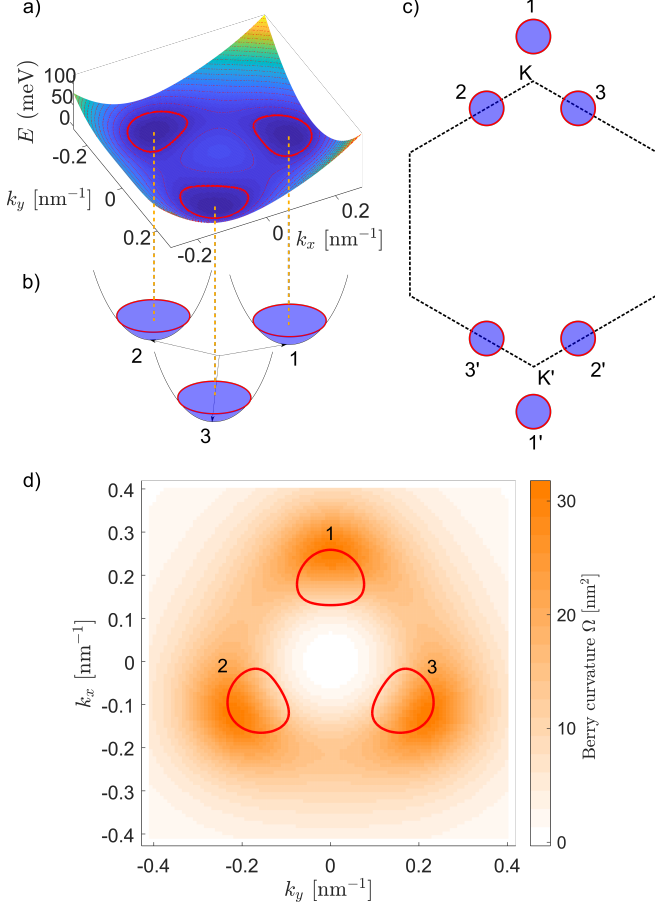


FIG. 2. The band structure and the effective three-pocket model. a) The low-energy model in the presence of trigonal warping leads to the emergence of three electron pockets at low electron densities, shown by solid red contours. b) A toy model that mimics the three-pocket band structure of the BLG. c) A schematic of the pockets positions near K and K' points. d) The distribution of the Berry curvature in the conduction band near K point. Here we used the parameters: $D = 100$ meV, $\mu = 90$ meV. The method of calculation is described in the Supplement.

$$H_i(\mathbf{p}) = \frac{(\mathbf{p} - \mathbf{p}_i)^2}{2m_*}, \quad (11)$$

where $i = 1, 2, 3$ labels the pockets, p_i are the centers of the pockets, corresponding to three minima of the up-

per band in field-biased BG. Their locations are $p_{*1} = p_*(0, 1)$, $p_{*2} = p_*(-\frac{\sqrt{3}}{2}, -\frac{1}{2})$, and $p_{*3} = p_*(\frac{\sqrt{3}}{2}, -\frac{1}{2})$. The values of momentum displacement p_* and the effective mass m_* of the pockets are extracted from realistic band structure [41].

In phase 1, there are three possible candidate ground states in which electrons fill up one, two or all three pockets. To determine which one of them is the true ground state, we compare their energies E_N ($N = 1, 2, 3$ is the number of occupied pockets) at the same total carrier density n . Their energies $E_N = E_K^{(N)} + E_{ex}^{(N)}$ consist of kinetic and exchange energy contributions. Using the fact that the density of states in each pocket is a constant $\nu_* = m_*/2\pi$, we can write the total kinetic energy as

$$E_K^{(N)} = \frac{N}{2\nu_*} \frac{n^2}{N^2} = \frac{\pi n^2}{Nm_*} \quad (12)$$

In order to explore the pocket polarization, we restore the momentum dependence of the interaction in the exchange part of the free energy:

$$E_{ex}^{(N)} = -\frac{1}{2} \sum_{i,j=1}^N \sum_{\mathbf{p}, \mathbf{p}'} V_{\mathbf{p}-\mathbf{p}'} n_{i\mathbf{p}} n_{j\mathbf{p}'}, \quad V_{\mathbf{p}-\mathbf{p}'} = \frac{2\pi e^2}{\kappa |\mathbf{p} - \mathbf{p}'|}. \quad (13)$$

where the quantity $n_{i\mathbf{p}}$ is the occupation number at momentum \mathbf{p} measured from the center of the pocket i . As a reminder, for simplicity, we introduced finite dielectric constant κ to represent the effect of screening. We note that when the carrier density is small, the inter-pocket exchange interaction has a nearly momentum-independent renormalization effect on the energy of each electron, which justifies approximating the Fermi surface in each pocket by a circle centered at p_{*i} . From this, we have

$$E_{ex}^{(N)} = -\frac{1}{2} \sum_{i,j=1}^N \sum_{\mathbf{p}, \mathbf{p}'} V_{\mathbf{p}-\mathbf{p}'+\mathbf{p}_{*i}-\mathbf{p}_{*j}} n_{i\mathbf{p}} n_{j\mathbf{p}'}, \quad (14)$$

where $\mathbf{p}_{ij} = \mathbf{p}_{*i} - \mathbf{p}_{*j}$ is the momentum difference between two pocket centers, $n_{\mathbf{p}}$ is the occupation number of the state with momentum \mathbf{p} measured from the center of an arbitrary pocket

$$n_{\mathbf{p}} = 1 - \Theta(|\mathbf{p}| - p_0) \quad (15)$$

where p_0 is the radius of the circular Fermi sea in each

pocket

$$p_0 = \sqrt{\frac{4\pi n}{N}}. \quad (16)$$

With these, we can proceed to evaluate the exchange energy analytically by performing the Fourier transform (see the Supplement). Eventually, we get

$$E_{ex}^{(N)} = -\frac{e^2 p_0^3}{16\pi} \sum_{ij} \int_0 \left[J_2(z) + J_0(z) \right]^2 J_0 \left(\frac{z|p_{ij}|}{p_0} \right) dz. \quad (17)$$

Let us discuss the validity of this scenario. The existence of three disconnected Fermi pockets requires $p_* \gg p_0$ where p_* is the momentum of at the center of each pocket measured from K point, and p_0 is the radius of each Fermi pocket. This yields an upper bound for carrier density: $n \lesssim 0.3 \times 10^{12} \text{ cm}^{-2}$, where we used the value of p_* estimated in the Supplement[41].

Below, we will focus on the pocket polarization on top of phase 1. From Fig. 1 a), we see that the maximal density in phase 1 always satisfies the validity requirement of our model. With this in mind, we can safely use the results of our pocket model, Eq. (12) and Eq. (17) to determine the phase diagram by comparing the total energy of one-pocket, two-pocket and three-pocket configurations numerically.

The resulting pocket polarization phase diagram in the small density regime is shown in Fig. 1 b). From this phase diagram, we find that electrons always prefer to cluster in one of the three pockets at a low carrier density. With the increase of carrier density, the system undergoes phase transitions into two-pocket and finally, into the pocket-unpolarized configuration. In Fig. 1 b), we set the dielectric constant to be $\kappa = 2$ for the purpose of presentation, so that the phase diagram showcases all possible phases. The phase diagram observed in experiments can vary from system to system, since the competition of pocket orders is sensitive to screening, which depends on the experiment setup. If, for example, due to a proximal gate, the screening effect is stronger than assumed in Fig. 1 b), then the pocket unpolarized state will be suppressed. Alternatively, if the screening in the experiment is weaker than assumed in our calculation, the pocket polarized phase in the phase diagram will expand. We note that the energy splitting between the ground-state configuration and two higher-energy states is at the order of 0.1meV to 1meV, corresponding to an ordering temperature of several Kelvin, which is accessible in experiments.

Finally, we discuss manifestations of momentum-polarized states. Individual pocket can of course be identified through the quantum oscillations e.g. of magnetoresistance. The oscillation frequency as a function of

inverse out-of-plane magnetic field measures the area of the Fermi surface. Taken relative to the net carrier density, the oscillation frequency will be reduced by a factor of $1/n$ once n pockets form.

Crucially, the pocket-polarized states further break the crystallographic symmetries, leading to distinct effects that can be probed by the symmetry-sensitive measurements discussed above. Indeed, two possible orders of the parent phase, i.e. phase 1, correspond to two kinds of broken symmetries— either breaking only mirror symmetry, or breaking rotation, mirror and translation symmetries (see Table I). If phase 1 only breaks mirror symmetry, then populating one or two out of three pockets will further break the three-fold rotation symmetry without breaking the translation symmetry, leading to electron nematicity. This symmetry breaking can be observed by measuring the anisotropy of the conductivity. If, however, the parent isospin order is intervalley coherent, then the only remaining symmetry to be broken in the pocket-polarization transition is the discrete translation symmetry. Namely, the pocket polarization on top of valley coherent states modifies the Kekulé charge density wave into an incommensurate Kekulé charge density wave which carries momentum $2K + p_{*i} + p_{*i'}$, $i = 1, 2, 3$, $p_{*i'} = -p_{*i}$, see Fig. 2 c). In this case, the pocket order can be detected by probing long-periodicity spatial modulation.

Pocket polarization can also be detected by measuring the Hall conductivity. When the pocket polarization happens on top of the valley imbalance order O_1^z which allows a nonvanishing Hall conductivity, the Hall conductivity changes abruptly since the Berry curvature is non-uniform near K point [see Fig. 2 d)]. If the pocket polarization occurs on top of O_1^{xy} isospin order, which originally respects the time reversal symmetry and enforces a vanishing Hall conductivity, then the onset of the pocket polarization can break the time-reversal symmetry so long as electrons populate different pockets in valleys K and K' [e.g. pocket 1 and 2' in Fig. 2 c)]. As a result, the Hall conductivity will jump from zero to some finite value at the pocket ordering transition. Therefore, regardless of the form of the parent isospin order, we always expect a discontinuous behavior in Hall conductance at the onset of pocket orders.

In conclusion, we predict that exchange interactions drive the pocket polarization that emerges on top of an isospin polarized phase in field-biased BG. This new order further breaks the crystallographic symmetries in the isospin polarized parent phase. Depending on the isospin orientation of the parent phase, the pocket polarization can either break the rotation symmetry or the translation symmetry, resulting in either nematic order or an incommensurate Kekulé density wave order. The new orders arise through phase transitions showing interesting interplay with the cascade of isospin-polarized phases seen in other seen in other flatband systems[26–33].

-
- [1] E. J. Mele, Commensuration and interlayer coherence in twisted bilayer graphene, *Phys. Rev. B* 81, 161405(R) (2010)
 - [2] Rafi Bistritzer and Allan H. MacDonald, Moiré bands in twisted double-layer graphene, *PNAS* 108, 30 (2011)
 - [3] Y. Cao, V. Fatemi, S. Fang, K. Watanabe, T. Taniguchi, E. Kaxiras, and P. Jarillo-Herrero, *Nature* 556, 43 (2018).
 - [4] Y. Cao, V. Fatemi, A. Demir, S. Fang, S. L. Tomarken, J. Y. Luo, J. D. Sanchez-Yamagishi, K. Watanabe, T. Taniguchi, E. Kaxiras, R. C. Ashoori, and P. Jarillo-Herrero, *Nature* 556, 80 (2018).
 - [5] J. Kang and O. Vafek, Strong coupling phases of partially filled twisted bilayer graphene narrow bands, *Phys. Rev. Lett.* 122, 246401 (2019)
 - [6] M. Xie and A. H. MacDonald, Nature of the correlated insulator states in twisted bilayer graphene, *Phys. Rev. Lett.* 124, 097601 (2020)
 - [7] M. Ochi, M. Koshino, and K. Kuroki, Possible correlated insulating states in magic-angle twisted bilayer graphene under strongly competing interactions, *Phys. Rev. B* 98, 081102(R) (2018)
 - [8] Ferromagnetic Mott state in twisted graphene bilayers at the magic angle, K. Seo, V. N. Kotov, and B. Uchoa, *Phys. Rev. Lett.* 122, 246402 (2019)
 - [9] F. Wu and S. Das Sarma, Ferromagnetism and superconductivity in twisted double bilayer graphene, *Phys. Rev. B* 101, 155149 (2020)
 - [10] F. Wu and S. Das Sarma, Collective Excitations of Quantum Anomalous Hall Ferromagnets in Twisted Bilayer Graphene, *Phys. Rev. Lett.* 124, 046403 (2020)
 - [11] A. L. Sharpe, E. J. Fox, A. W. Barnard, J. Finney, K. Watanabe, T. Taniguchi, M. A. Kastner, D. Goldhaber-Gordon, Emergent ferromagnetism near three-quarters filling in twisted bilayer graphene, *Science*, 365, 6453, 605-608 (2019)
 - [12] M. Serlin, C. L. Tschirhart, H. Polshyn, Y. Zhang, J. Zhu, K. Watanabe, T. Taniguchi, L. Balents, A. F. Young, Intrinsic quantized anomalous Hall effect in a moiré heterostructure. *Science*, 367, 6480 (2020)
 - [13] C. L. Tschirhart, M. Serlin, H. Polshyn, A. Shragai, Z. Xia, J. Zhu, Y. Zhang, K. Watanabe, T. Taniguchi, M. E. Huber, A. F. Young, Imaging orbital ferromagnetism in a moiré Chern insulator, *Science*, 372, 6548, (1323-1327), (2021).
 - [14] J. F. Dodaro, S. A. Kivelson, Y. Schattner, X. Q. Sun, and C. Wang, Phases of a phenomenological model of twisted bilayer graphene, *Phys. Rev. B* 98, 075154 (2018)
 - [15] S. Liu, E. Khalaf, J. Y. Lee, and A. Vishwanath, "Nematic topological semimetal and insulator in magic angle bilayer graphene at charge neutrality," *Phys. Rev. Research* 3, 013033 (2021).
 - [16] A. Kerelsky, L. McGilly, D. M. Kennes, L. Xian, M. Yankowitz, S. Chen, K. Watanabe, T. Taniguchi, J. Hone, C. Dean, A. Rubio, and A. N. Pasupathy, *Nature* 572, 95 (2019).
 - [17] Y. Choi, J. Kemmer, Y. Peng, A. Thomson, H. Arora, R. Polski, Y. Zhang, H. Ren, J. Alicea, G. Refael, F. von Oppen, K. Watanabe, T. Taniguchi, and S. Nadj-Perge, *Nat. Phys.* 15, 1174 (2019).
 - [18] Y. Jiang, X. Lai, K. Watanabe, T. Taniguchi, K. Haule, J. Mao, and E. Y. Andrei, *Nature* 573, 91 (2019).
 - [19] Y. Cao, D. R. Legrain, J. M. Park, F. N. Yuan, K. Watanabe, T. Taniguchi, R. M. Fernandes, L. Fu, P. Jarillo-Herrero, arXiv:2004.04148 (2020).
 - [20] F. Guinea and N. R. Walet, Electrostatic effects, band distortions, and superconductivity in twisted graphene bilayers, *PNAS* 115 (52) 13174-13179 (2018)
 - [21] H. Isobe, N. F. Q. Yuan, and L. Fu, Unconventional Superconductivity and Density Waves in Twisted Bilayer Graphene, *Phys. Rev. X* 8, 041041 (2018)
 - [22] V. Kozii, H. Isobe, J. W. F. Venderbos, and L. Fu, Nematic superconductivity stabilized by density wave fluctuations: Possible application to twisted bilayer graphene, *Phys. Rev. B* 99, 144507 (2019)
 - [23] C. Xu and L. Balents, Topological Superconductivity in Twisted Multilayer Graphene, *Phys. Rev. Lett.* 121, 087001 (2018)
 - [24] Y.-P. Lin and R. M. Nandkishore, Chiral twist on the high-Tc phase diagram in moiré heterostructures, *Phys. Rev. B* 100, 085136 (2019)
 - [25] H. Zhou, Y. Saito, L. Cohen, W. Huynh, C. Patterson, F. Yang, T. Taniguchi, K. Watanabe, and A. F. Young, Isospin magnetism and spin-triplet superconductivity in Bernal bilayer graphene, arXiv: 2110.11317
 - [26] H. Zhou, T. Xie, A. Ghazaryan, T. Holder, J. R. Ehrets, E. M. Spanton, T. Taniguchi, K. Watanabe, E. Berg, M. Serbyn, A. F. Young. Half and quarter metals in rhombohedral trilayer graphene, arXiv:2104.00653.
 - [27] V. Cvetkovic, O. Vafek, Topology and symmetry breaking in ABC trilayer graphene, arXiv:1210.4923.
 - [28] Y. Lee, S. Che, J. Velasco Jr., D. Tran, J. Baima, F. Mauri, M. Calandra, M. Bockrath, C. N. Lau, Gate Tunable Magnetism and Giant Magnetoresistance in ABC-stacked Few-Layer Graphene, arXiv:1911.04450
 - [29] Y. Saito, F. Yang, J. Ge, et al. Isospin Pomeranchuk effect in twisted bilayer graphene. *Nature* 592, 220–224 (2021).
 - [30] U. Zondiner, A. Rozen, D. Rodan-Legrain, et al. Cascade of phase transitions and Dirac revivals in magic-angle graphene. *Nature* 582, 203–208 (2020).
 - [31] A. Rozen, J. M. Park, U. Zondiner, et al. Entropic evidence for a Pomeranchuk effect in magic-angle graphene. *Nature* 592, 214–219 (2021).
 - [32] Y. Choi, H. Kim, Y. Peng, et al. Correlation-driven topological phases in magic-angle twisted bilayer graphene. *Nature* 589, 536–541 (2021).
 - [33] A. T. Pierce, Y. Xie, J. M. Park, E. Khalaf, S. H. Lee, Y. Cao, D. E. Parker, P. R. Forrester, S. Chen, K. Watanabe, T. Taniguchi, A. Vishwanath, P. Jarillo-Herrero, A. Yacoby, Unconventional sequence of correlated Chern insulators in magic-angle twisted bilayer graphene, arXiv: 2101.04123
 - [34] M. Koshino and E. McCann, Trigonal warping and Berry's phase $N\pi$ in ABC-stacked multilayer graphene, *Phys. Rev. B* 80, 165409 (2009).
 - [35] F. Zhang, B. Sahu, H. Min, and A. H. MacDonald, Band structure of ABC-stacked graphene trilayers, *Phys. Rev. B* 82, 035409 (2010)
 - [36] A. S. Mayorov, D. C. Elias, M. Mucha-Kruczynski, R. V. Gorbachev, T. Tudorovskiy, A. Zhukov, S. V. Morozov, M. I. Katsnelson, V. I. Fal'ko, A. K. Geim, and K. S. Novoselov, *Science* 333, 860 (2011).

- [37] J. Velasco Jr., L. Jing, W. Bao, Y. Lee, P. Kratz, V. Aji, M. Bockrath, C. N. Lau, C. Varma, R. Stillwell, D. Smirnov, F. Zhang, J. Jung, and A. H. MacDonald, Nat. Nanotechnol. 7, 156 (2012).
- [38] R. E. Throckmorton and S. Das Sarma, Quantum multicriticality in bilayer graphene with a tunable energy gap Phys. Rev. B 90, 205407 (2014)
- [39] J. Jung, M. Polini, and A. H. MacDonald, Persistent current states in bilayer graphene, Phys. Rev. B 91, 155423 (2015)
- [40] E. McCann and M. Koshino, Rep. Prog. Phys. 76 056503 (2013)
- [41] See Supplementary Information.

SUPPLEMENTARY INFORMATION

A. Field-biased bilayer graphene bandstructure

1. Two-band single-particle Hamiltonian

The two-layer model is derived [34] under the assumption that intra- and interlayer hoppings (A1B1 and A2B1-type terms in the original Hamiltonian, which are 3.16 eV and 0.38 eV, correspondingly) are much larger than all the other energy scales. The single-particle Hamiltonian can be written as:

$$H_0 = \sum_{\mathbf{p}} \psi_i^\dagger [h_0 + h_t + h_a + h_{D'}]_{ij} \psi_j \quad (\text{S1})$$

$$h_0 = h_1(\mathbf{p})\Sigma_1 + h_2(\mathbf{p})\Sigma_2 + D\sigma_3 \quad (\text{S2})$$

$$h_t = v_3 (p_2\Lambda_1 + p_1\Lambda_2) \quad (\text{S3})$$

$$h_a = \frac{1}{2m_a} p^2 \quad (\text{S4})$$

$$h_{D'} = -D \frac{p^2}{p_D^2} \sigma_3 \quad (\text{S5})$$

Note that we rotated the basis by 90° with respect to ref. [34]. Here h_0 is the minimal model Hamiltonian that we start our consideration from in Eq. (1). h_t produces the trigonal warping; h_a produces the particle-hole asymmetry and $h_{D'}$ is the momentum-dependent contribution that is proportional to the displacement field. The matrices are:

$$\Sigma_1 = \sigma_1, \Sigma_2 = \tau_3\sigma_2, \Lambda_1 = \tau_3\sigma_1, \Lambda_2 = \sigma_2 \quad (\text{S6})$$

$$(\text{S7})$$

and the coefficients of h_0 can be written as:

$$h_1(\mathbf{p}) = -\frac{1}{2m} (p_2^2 - p_1^2) \quad (\text{S8})$$

$$h_2(\mathbf{p}) = \frac{1}{2m} (2p_1p_2). \quad (\text{S9})$$

We measure the energies in meV and the momentum is made dimensionless by multiplying by the carbon-carbon atom distance $a_{CC} = 1.46$ Å. The parameters are tabulated in Tab.II.

2. Projection on the conduction band

The projection to conduction band discussed in main text is formally written as following transform:

$$M \rightarrow \tilde{M} = \text{tr}_\sigma(\hat{P}M), \quad (\text{S10})$$

where tr_σ is the partial trace over sublattice degrees of freedom, the projection operator \hat{P} is defined as

$$\hat{P} = \frac{1}{2} \left(\frac{h_0(\mathbf{p})}{E(\mathbf{p})} + 1 \right), \quad E(\mathbf{p}) = \sqrt{D^2 + \left(\frac{p^2}{2m} \right)^2}. \quad (\text{S11})$$

parameter	value	parameter	value
a	2.46 Å	v	1.1×10^6 m/s
γ_0	3.16 eV	v_3	1.3×10^5 m/s
γ_1	0.381 eV	v_4	4.8×10^4 m/s
γ_3	0.38 eV	m	$0.028 m_e$
γ_4	0.14 eV	m_a	$0.19 m_e$
D	0 – 100 meV	p_{DACC}	0.058

TABLE II. Parameters in the Hamiltonian computed based on values in ref. [34]. The velocities are defined as $v_i = \frac{\sqrt{3}a\gamma_i}{2\hbar}$. The mass is defined as $m = \frac{\gamma_1}{2v^2}$, and the anisotropy mass is determined from $\frac{1}{2m_a} = \frac{2vv_4}{\gamma_1} + \frac{\Delta'v^2}{\gamma_1^2}$, where $\Delta = 22\text{meV}$.

After projection, the single-particle part of the minimal model Hamiltonian becomes diagonal

$$\tilde{H}_0 = \sum_{i\mathbf{p}} E(\mathbf{p}) \tilde{\psi}_{i,\mathbf{p}}^\dagger \tilde{\psi}_{i,\mathbf{p}}, \quad i = K \uparrow, K \downarrow, K' \uparrow, K' \downarrow \quad (\text{S12})$$

where $\tilde{\psi}_{i,\mathbf{p}}$ is the field operator of conduction band electrons in two valleys and two spins. From now on, we write the spin indices explicitly.

In this paper, we focus on the effect of electron-electron interaction, which we modeled as a density-density coupling:

$$H_{int} = \sum_{\mathbf{p}\mathbf{p}'\mathbf{q}} V_{\mathbf{q}} \psi_{i,\mathbf{p}}^\dagger \psi_{j,\mathbf{p}'}^\dagger \psi_{j,\mathbf{p}'-\mathbf{q}} \psi_{i,\mathbf{p}+\mathbf{q}} \quad (\text{S13})$$

At large D , the form of density-density interaction is invariant under projection:

$$\tilde{H}_{int} = \sum_{\mathbf{p}\mathbf{p}'\mathbf{q}} V_{\mathbf{q}} \tilde{\psi}_{i,\mathbf{p}}^\dagger \tilde{\psi}_{j,\mathbf{p}'}^\dagger \tilde{\psi}_{j,\mathbf{p}'-\mathbf{q}} \tilde{\psi}_{i,\mathbf{p}+\mathbf{q}} \quad (\text{S14})$$

Here, same as in Eq.(S12), i and j .

3. Three-pocket model

In this section, we explain how we extract the parameters p_* and m_* we used in three-pocket model from the realistic BG band structure. As we only care about the band dispersion near the band minima, we model the three-pocket band structure using three isotropic parabolic bands:

$$H_i(\mathbf{p}) = \frac{(\mathbf{p} - \mathbf{p}_i)^2}{2m_*}, \quad i = 1, 2, 3 \quad (\text{S15})$$

where i labels the pockets, \mathbf{p}_i 's are the centers of pockets, corresponding to three minima of the conduction band:

$$\mathbf{p}_{*1} = p_*(0, 1), \quad \mathbf{p}_{*2} = p_*(-\frac{\sqrt{3}}{2}, -\frac{1}{2}), \quad \mathbf{p}_{*3} = p_*(\frac{\sqrt{3}}{2}, -\frac{1}{2}). \quad (\text{S16})$$

where we specify the values of p_* and m_* below.

In order to relate the three-pocket bandstructure represented by three parabolas to the single-particle bandstructure shown before, we first adopt a minimal model that possesses three pockets at large displacement field D . This model has the Hamiltonian

$$H_{3-p}^{min} = \sum_{\mathbf{p}} \psi_{i\mathbf{p}}^\dagger [h_0(\mathbf{p}) + h_i(\mathbf{p}) + h_{D'}(\mathbf{p})]_{ij} \psi_{j\mathbf{p}} \quad (\text{S17})$$

We find the value of p_* by expanding in large D and treating the trigonal warping term perturbatively:

$$p_*(D) \approx p_D \left(\frac{4}{75} \frac{E_D}{D} + \frac{4}{5} \frac{D}{E_D} \right), \quad E_D = \frac{p_D^2}{2m} \approx 0.2 \text{ eV}, \quad (\text{S18})$$

In the main text, we used the expression $p_*(D)$ given in Eq.(S18) when numerically computing phase diagram. But when estimating the validity condition of toy model, we used the value of p_* at $D = 100\text{meV}$ for simplicity, which is $p_*(100\text{meV}) \approx 0.03/a_{CC}$.

The mass m_* is a parameter that we introduced in the three-pocket toy model to mimic the bottom of the conduction band from (S17). As we are interested in instabilities, the most important quantity we need to mimic with toy model is the density of states. Therefore, below, we determine the value of m_* in our toy model so that it reproduces the density of states of the original model. The Hamiltonian Eq.(S17) near one of the minimum takes the following form

$$H(\mathbf{p}_{*1} + \delta\mathbf{p}) = \frac{\delta p_x^2}{2m_{*\perp}} + \frac{\delta p_y^2}{2m_{*\parallel}} \quad (\text{S19})$$

where

$$m_{*\parallel} = 0.57m \frac{E_D D}{0.07E_D^2 + D^2}, \quad m_{*\perp} = \frac{0.18p_D}{v_3} \quad (\text{S20})$$

The density of states in the model (S17) is given by

$$\nu = \frac{1}{2\pi} \sqrt{m_{*\perp} m_{*\parallel}}. \quad (\text{S21})$$

Therefore, to reproduce the same density of states in our toy model Eq.(11), we set $m_* = \sqrt{m_{*\perp} m_{*\parallel}}$.

B. Exchange energy in three-pocket model

In this section, we calculate the exchange energy, which takes the form of a convolution:

$$E_{ex}^{(N)} = - \sum_{i,j=1}^N \sum_{\mathbf{p}, \mathbf{p}'} V_{\mathbf{p}-\mathbf{p}'} n_{i\mathbf{p}} n_{j\mathbf{p}'} = - \sum_{i,j=1}^N \sum_{\mathbf{p}, \mathbf{p}'} V_{\mathbf{p}-\mathbf{p}'+\mathbf{p}_{ij}} n_{\mathbf{p}} n_{\mathbf{p}'}, \quad V_{\mathbf{p}-\mathbf{p}'} = \frac{2\pi e^2}{|\mathbf{p}-\mathbf{p}'|}, \quad n_{\mathbf{p}} = 1 - \Theta(|p| - p_0). \quad (\text{S22})$$

where $\mathbf{p}_{ij} = \mathbf{p}_{*i} - \mathbf{p}_{*j}$ is the momentum difference between two pocket centers. We compute this quantity by performing Fourier transform:

$$V(x) = \frac{e^2}{|x|} \quad (\text{S23})$$

and

$$n(x) = \sum_{\mathbf{p}} e^{i\mathbf{p} \cdot \mathbf{x}} n_{\mathbf{p}} \quad (\text{S24})$$

Then, the exchange energy can be written as

$$E_{ex}^{(N)} = \frac{1}{2} \sum_{ij} \int d^2x V(x) n(\mathbf{x})^2 e^{i\mathbf{p}_{ij} \cdot \mathbf{x}} = \frac{1}{2} \sum_{ij} \int_0^{\frac{\pi}{2}} V(x) n(x)^2 2\pi J_0(x|p_{ij}|) x dx \quad (\text{S25})$$

To calculate this quantity, we need to first work out the form of $n(x)$:

$$n(x) = \int_{|p| < p_0} \frac{dp_x dp_y}{4\pi^2} e^{ip_x x} = \int \frac{dp_x}{2\pi^2} \sqrt{p_0^2 - p_x^2} e^{ip_x x} = \frac{p_0^2}{2\pi^2} \int_{-\frac{\pi}{2}}^{\frac{\pi}{2}} d\theta \cos^2 \theta e^{iz \sin \theta} \quad (\text{S26})$$

$$= \frac{p_0^2}{8\pi} [J_2(z) + 2J_0(z) + J_{-2}(z)] = \frac{p_0^2}{4\pi} [J_2(z) + J_0(z)] \quad (\text{S27})$$

where $z = xp_0$

$$E_{ex}^{(N)} = -\frac{e^2 p_0^3}{16\pi} \sum_{ij} \int_0^{\frac{\pi}{2}} dz [J_2(z) + J_0(z)]^2 J_0\left(\frac{z|p_{ij}|}{p_0}\right) \quad (\text{S28})$$

C. Estimation of interaction strength V

In the main text, we need to use the value of V , which represent the strength of exchange interaction, when numerically calculating the phase diagram. Here, we estimate the realistic value of V .

The interaction strength we used in our model in main text should correspond to the strength of the screened Coulomb interaction at the relevant momentum, which is Fermi momentum p_0 , i.e.

$$V = \tilde{V}_{p_0}. \quad (\text{S29})$$

Accounting for Thomas-Fermi screening, the screened Coulomb potential takes the following form

$$\tilde{V}_{p_0} = \frac{V_{p_0}}{1 + V_{p_0} \Pi_{p_0}}, \quad (\text{S30})$$

where Π_{p_0} is the polarization function at Fermi momentum. We estimate this quantity using the value of density of states at Fermi surface ν_0 . When the band is flat compared to the interaction energy, which is the case of our interest, we have

$$\nu_0 V_{p_0} \gg 1 \quad (\text{S31})$$

In this regime, the screened Coulomb interaction is approximately

$$\tilde{V}_{p_0} = \frac{1}{\nu_0}. \quad (\text{S32})$$

Therefore, we can estimate the interaction as

$$V \sim \frac{1}{\nu_0} \sim 10^3 \text{meVnm}^2 \quad (\text{S33})$$

where we have used $\nu_0 \sim n/W \sim 10^{-3} \text{meV nm}^{-2}$, where n is the carrier density $n \sim 10^{12} \text{cm}^{-2}$, W is the Fermi energy measured from band bottom at that carrier density $W \sim 10 \text{meV}$.

D. Berry curvature

It is straight forward to compute the Berry curvature using the Hamiltonian Eq. (S17). In this section, we explain how we compute the Berry curvature in realistic BG model and obtain the result of Fig.2. We take the form of the Hamiltonian projected to conduction band in Eq. (S17), and rewrite it as

$$H_{3-p}^{min} = \sum_{\mathbf{p}} \psi_{i\mathbf{p}}^\dagger \mathbf{h}(\mathbf{p}) \cdot \boldsymbol{\tau}_{ij} \psi_{j\mathbf{p}}, \quad \mathbf{h}(\mathbf{p}) \cdot \boldsymbol{\tau} = [h_0(\mathbf{p}) + h_t(\mathbf{p}) + h_{D'}(\mathbf{p})] \quad (\text{S34})$$

where $\boldsymbol{\tau} = (\tau_1, \tau_2, \tau_3)$. Then the Berry curvature is given by

$$\Omega = \frac{1}{2} \frac{\mathbf{h}}{|\mathbf{h}|} \cdot \left(\frac{\partial \mathbf{h}(\mathbf{p})}{\partial p_1} \times \frac{\partial \mathbf{h}(\mathbf{p})}{\partial p_2} \right). \quad (\text{S35})$$
